

Hierarchical Al-doped and Hydrogenated ZnO Nanowire@MnO₂ Ultra-Thin Nanosheet Core/Shell Arrays for High-Performance Supercapacitor Electrode

Mingpeng Yu^{1,2}, Hongtao Sun², Xiang Sun², Fengyuan Lu², Gongkai Wang², Tao Hu², Hong Qiu¹ and Jie Lian^{2,*}

¹ Department of Physics, School of Mathematics and Physics, University of Science and Technology Beijing, 30 Xueyuan Road, Haidian District, Beijing 100083, China

² Department of Mechanical, Aerospace & Nuclear Engineering, Rensselaer Polytechnic Institute, Troy, New York, 12180, USA

*E-mail: LIANJ@rpi.edu

Received: 16 October 2012 / Accepted: 7 December 2012 / Published: 1 February 2013

ZnO@MnO₂ and Al-doped ZnO (AZO)@MnO₂ hybrid electrodes in core/shell geometries have been synthesized on stainless steel substrates by a scalable low-cost solution route. Cyclic voltammogram (CV) and galvanostatic (GV) charge-discharge measurements demonstrated that the AZO@MnO₂ hybrid electrode exhibited superior capacitive properties, in 1M Na₂SO₄ aqueous solution, to the ZnO@MnO₂ electrode. The specific capacitance based on total electrode mass is estimated to be 275 F/g at a current density of 2 A/g. The AZO@MnO₂ electrode also displays an excellent long-term cyclic stability at a current density of 10 A/g with less than 3% loss after 2000 charge-discharge cycles. A ~35% capacity retention was observed at 60A/g, which is over 400% specific capacitance increment compared with the ZnO@MnO₂ electrode. The superior electrochemical capacitive properties of the AZO@MnO₂ over ZnO@MnO₂ can be attributed to the enhanced electrical conductivity in the core nanowire, as a result of Al doping and hydrogenation. The low cost fabrication combined with the excellent capacitive properties indicates that the AZO@MnO₂ hybrid architecture can serve as a promising electrode material for supercapacitors as well as other electrochemical energy storage/conversion devices.

Keywords: ZnO nanowires, MnO₂, core/shell hybrid architecture, supercapacitors, energy storage

1. INTRODUCTION

The development of high performance electrode materials is critical for advanced energy storage systems including supercapacitors and batteries in delivering simultaneously high energy

density and power density. It was reported that 90% of the capacitor cost resides in the electrode material [1], and it is a challenge to find high performance electrode materials (i.e., high specific capacitance as well as good rate capability) accompanied with low-cost, environmental benignity and natural abundance. Three main categories of electrode materials are typically employed including carbonaceous materials [2,3], conducting polymers [4,5], and metal oxides/hydroxides [6,7]. Among various metal oxide/hydroxides electrodes, hydrous RuO_2 is the state-of-the-art pseudocapacitor material with a specific capacitance as high as 1300 F/g [7]. However, the high cost and environmental toxicity of Ru as well as use of strong acidic electrolytes limit its practical applications. MnO_2 , a nontoxic 3d transition metal oxide with a high theoretical capacitance up to 1370 F/g, has attracted much attention due to its low cost, good electrochemical reactivity, environmentally-friendly property and enhanced safety during operations. Although MnO_2 has been considered to be one of the most attractive alternative to RuO_2 ; however, the low electrical conductivity (in the range of 10^{-5} - 10^{-6} S/cm) and poor rate performance of MnO_2 electrodes have been their major challenges, limiting the rate capabilities for high power and cycling performances. The achievable capacitance is highly dependent on morphology, specific surface area and electrical conductivity [8].

For various energy storage architectures, nanostructured electrode materials are very useful in facilitating mass transport, ion diffusion and electron transfer and thereby improving electrochemical performances [9-13]. In order to improve the electrical conductivity of MnO_2 -based electrodes, various MnO_2 -conductive matrix (*carbonaceous materials* [14-19] and conducting polymers [20-22]) hybrid nanostructures have been proposed as suitable approaches to boost the electrochemical performance. These methods could enhance the electrical conductivity and increase the active sites as well as the homogeneity of the electrochemical reaction, thus improving electrochemical performance of the electrode materials. Particularly, novel nanostructured electrodes based on 1D nanowire/nanorod arrays have attracted considerable attentions due to the synergic effect of the core/shell structures. By constructing hierarchical core/shell structures with porous electroactive materials to improve high transport rates of electrolyte ions and electrons, high specific capacitance have been obtained. For example, hybrid nanostructures of $\text{Co}_3\text{O}_4@\text{MnO}_2$ [23], $\text{CoO}@\text{NiHON}$ [24], $\text{Zn}_2\text{SnO}_4@\text{MnO}_2$ [25], $\text{SnO}_2@\text{MnO}_2$ [26], $\text{CNT}@\text{RuO}_2$ [27] have been investigated for supercapacitor applications and improved performances have been demonstrated.

ZnO is a versatile material that can be easily fabricated with extremely low cost, and recently, much effort has been put into the development of one-dimensional (1D) ZnO nanowire/nanorod array-supported electrodes for electrochemical supercapacitors [28-30], utilizing its good electrical conductivity. However, due to its intrinsic semiconductor in nature, it is possible to further increase electrical conductivity of the ZnO nanowire/nanorod array-supported core/shell electrodes for more effective ion diffusion and electron transfer and enhance energy and power densities [31]. 1D ZnO nanowire with an appropriate amount of Al doping could provide an effective and facile way to increase the electrical conductivity by more than two orders of magnitudes [32]. Furthermore, post-growth hydrogen treatment is another simple and efficient method for the conductivity enhancement, which were intensively investigated both theoretically and experimentally [33-36]. The conductivity of ZnO could be enhanced by up to three orders of magnitude without significant changes in the structure and crystal orientation of the wurtzite type ZnO nanostructures [36]. Additionally, annealing in a

reducing atmosphere could also improve the conductive stability [37]. The approach of hydrogenation was also applied in other transition metal oxides such as SnO₂ and TiO₂ electrodes exhibiting more favorable electrochemical reactivity [38-40]. Very recently, Lu et al. [41] reported that hydrogenated TiO₂ nanotube arrays served as a good scaffold to support MnO₂ nanoparticles, leading to a specific capacitance of 912 F/g at a scan rate of 10 mV/s (based on the mass of MnO₂ only).

Here, we report, for the first time, a approach in synergizing the Al-doping and hydrogenation of the ZnO nanowires (hereafter referred to as AZO) to support redox active MnO₂ nanoshell electrodes in a core/shell geometry. This unique core/shell hybrid architecture displays several distinct advantages as electrode materials such as: (1) single-crystalline quality AZO nanowires (see Supplementary Information) serving as continuous electron transport pathways enabling faster electron transferring; (2) AZO nanowires directly grown on the stainless steel current collector, thus avoiding the use of polymer binder and conductive additives; (3) nanoporous ultrathin MnO₂ nanosheets facilitating ion diffusion and enabling a fast and reversible faradic reaction; and (4) core/shell geometries offer large electrochemically active area and enhanced electron collection efficiency, effectively combining high energy with high power characteristics (e.g., high specific capacity, good rate capability and long cycle life).

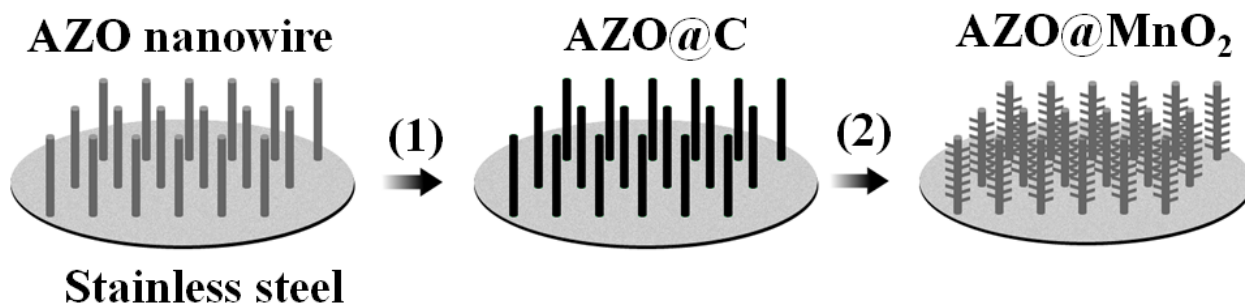
By combining unique properties of individual constituents, much improved electrochemical performance has been demonstrated for the AZO@MnO₂ as compared with the control electrode without Al-doping and hydrogenation. The specific capacitance can reach 275 F/g at a current density of 2 A/g (based on total electrode mass) and at 60 A/g, ~35% capacity retention can be achieved. The hybrid AZO/MnO₂ core/shell electrode also displays remarkable rate capability and an excellent long term cycle stability, promising for high performance supercapacitor applications. In addition, theoretical calculations suggest that transition metal oxides possessing prominent theoretical capacitance but more or less of low conductivity, such as TiO₂, SnO₂, Fe₂O₃, WO₃, CuO, Ag₂O, Cr₂O₃, even IrO₂ and RuO₂, could become more conductive upon the hydrogenation of the host lattice [42]. Therefore, the hydrogenation approach reported here can be applicable to a wide range of energy-storage electrode materials in improving the conductivity and enhancing their higher specific capacitance and specific power.

2. EXPERIMENTAL SECTION

2.1 Synthesis of ZnO@MnO₂ and AZO@MnO₂ nanowire arrays

All chemical reagents were purchased from Sigma-Aldrich and used without further purification. A two-step solution-based method was used for the fabrication of the core/shell hybrid architecture, as illustrated in Scheme 1. Firstly, AZO and ZnO nanowire arrays grown directly on stainless steel substrates were fabricated by a facile hydrothermal method (see Supplementary Information). The AZO and ZnO nanowire arrays were then subjected to overnight immersion in a 0.04 M aqueous glucose solution, followed by a 3-hour post-annealing at 450°C in 4% H₂ (balanced with Ar) and pure Ar gases, respectively. For the AZO nanowire array, carbonization and

hydrogenation processes were achieved in one single treatment step. Secondly, the AZO@C and ZnO@C nanowire arrays were immersed into a 0.03 M KMnO₄ solution and sealed in a Teflon-lined stainless steel autoclave at 160 °C for 5 hours.



Scheme 1. Schematic illustration of the fabrication processes of the hybrid electrode: (1) Carbon coating; and (2) chemical reaction between carbon and KMnO₄.

The reaction between carbon and KMnO₄ could lead to *in situ* formation of porous ultrathin MnO₂ nanosheets on AZO and ZnO nanowire arrays [23,43,44] based on the following reaction:



2.2 Structural characterization

The morphologies and microstructure of the as-prepared products were characterized by field emission scanning electron microscopy (FESEM, Zeiss 1540 EsB), X-ray diffraction (XRD; PANalytical) at room temperature with Cu K α radiation (wavelength = 1.54 Å), Raman spectroscopy (Renishaw, 514 nm) and transmission electron microscopy (TEM, JEOL 2010) operated at 200 keV. The chemical state of the products was characterized by X-ray photoelectron spectroscopy (XPS, PHI 5000 Versa Probe).

2.3 Electrochemical measurements

The electrochemical measurements of cyclic voltammograms (CV) and galvanostatic charge/discharge were conducted on an electrochemical workstation (Ametek, Princeton Applied Research, Versa STAT 4) using a three-electrode configuration in a 1M Na₂SO₄ solution. AZO@MnO₂ and ZnO@MnO₂ hybrid arrays on stainless steel substrates were used as working electrodes directly. The reference electrode and counter electrode were SCE (saturated calomel electrode) and platinum wire, respectively. CV tests were carried out over a voltage range of 0 to 0.8V vs. SCE at various scan rates from 10 to 400 mV/s. Galvanostatic charge/discharge measurements were conducted between 0 and 0.8 V vs. SCE at different current densities of 2-60 A/g.

3. RESULTS AND DISCUSSION

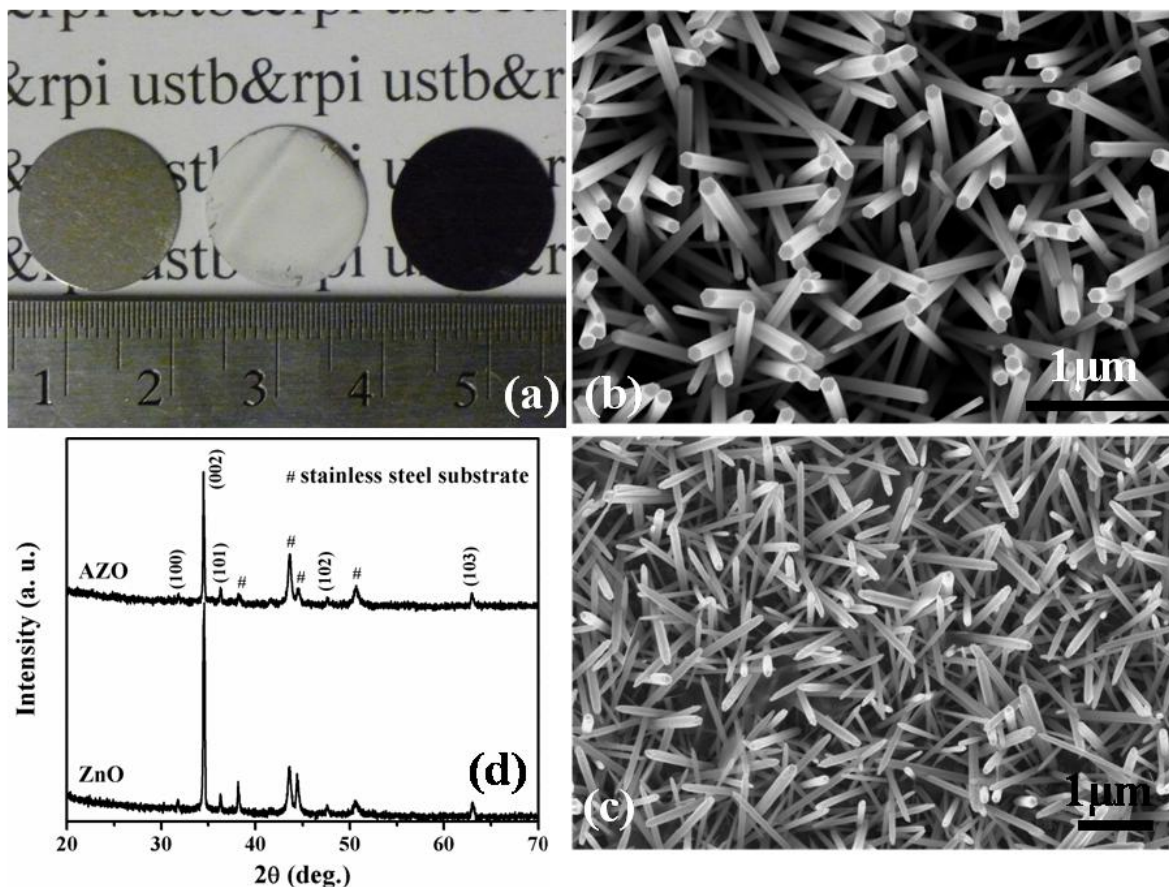


Figure 1. (a) Optical images of stainless steel (SS) substrate (left), AZO nanowire array on SS (middle) and AZO@MnO₂ hybrid electrode on SS (right); (b-c) SEM images of the ZnO and AZO nanowire arrays on SS, respectively; and (d) XRD patterns of the ZnO and AZO nanowire arrays.

Fig. 1(a) shows optical images of a bare 0.5 inch diameter stainless steel substrate (left), ZnO nanowire array on SS (middle) and AZO@MnO₂ on SS (right). The color changed from white to dark yellow reveals highly uniform thin films obtained. Fig. 1(b) and (c) show the FESEM images of the ZnO and AZO nanowire arrays obtained by the hydrothermal method. The diameter and the length of the ZnO nanowires were around 100 nm and 2 micrometer, respectively. Both ZnO and AZO nanowire arrays are well aligned on the substrate. The tops of the pure ZnO nanowire arrays were well-defined hexagons, indicating perfect hexagonal wurtzite structure; whereas AZO nanowire arrays are hexagon-like with irregular edge profiles, probably due to the effect of Al doping. Fig. 1(d) shows the XRD patterns of the ZnO and AZO nanowire arrays. No metallic Zn or Al characteristic peaks are observed. Both products exhibit the same growth direction along [001] orientation, indicating Al-doping in ZnO nanowires does not affect crystal orientation, the physical dimensions and microstructure of the ZnO nanowires.

In order to investigate chemical state of Al and the chemical composition of AZO nanowires, XPS measurement was conducted. The XPS survey spectrum from 100 to 1500 eV reveals the

presence of Zn, O, Al and C, as shown in Fig. 2(a). The C signal may originate from adventitious carbon contamination. The binding energy of Al-O for Al2p peak (74.6 eV) was clearly observed, as shown in Fig. 2(b).

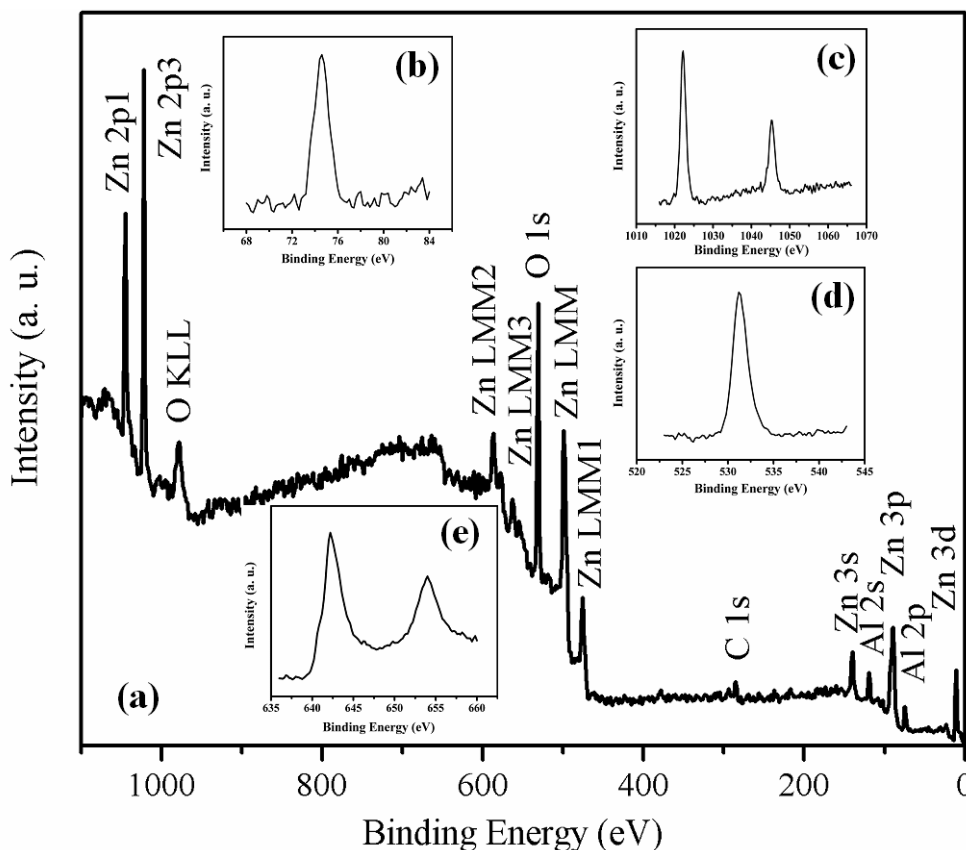


Figure 2. XPS results of the AZO nanowire arrays: (a) survey scan spectra; (b) Al 2p spectra; (c) Zn 2p spectra; (d) O 1s spectra; and (e) XPS spectra of Mn 2p of the AZO/MnO₂.

Moreover, the Al 2p peak exhibits a symmetry feature with a FWHM of 1.57 eV, and no metallic aluminum peak centered at 72.7 eV appears in the spectrum [45]. The one valence state of Al³⁺ indicates that Al elements have been successfully doped into the ZnO nanowire lattice. Zn 2p and O 1s spectra are drawn in Fig. 2(c) and (d), respectively. It can be seen that the XPS peak positions of Zn 2p_{3/2} and Zn 2p_{1/2} are centered at about 1021.9 and 1044.6 eV, respectively, demonstrating the Zn is a +2 valence state. The binding energy of O 1s is in good agreement with the literature values [46]. Both spectra are narrow and symmetrical and can be fitted with only one peak.

Fig. 3(a) shows the XRD pattern of AZO@MnO₂, in which one diffraction peak can be indexed to the birnessite-type MnO₂ (JCPDS card No. 80-1098) in addition to those from ZnO and the substrate. XRD revealed distinct yet broad peaks at $2\theta = 12.2^\circ$ which can be assigned to the (001) plane of a crystalline birnessite-type MnO₂ [47]. It is probable that the other diffraction peaks of the MnO₂ nanosheets are too weak to be observed due to the strong and sharp diffraction peaks of the SS substrate. The low intensity and broadening of the diffraction peak also suggest the small grain size

and poor crystallinity of the MnO_2 , which can be confirmed by the TEM results. Fig. 3(b) shows the Raman spectra of AZO@ MnO_2 .

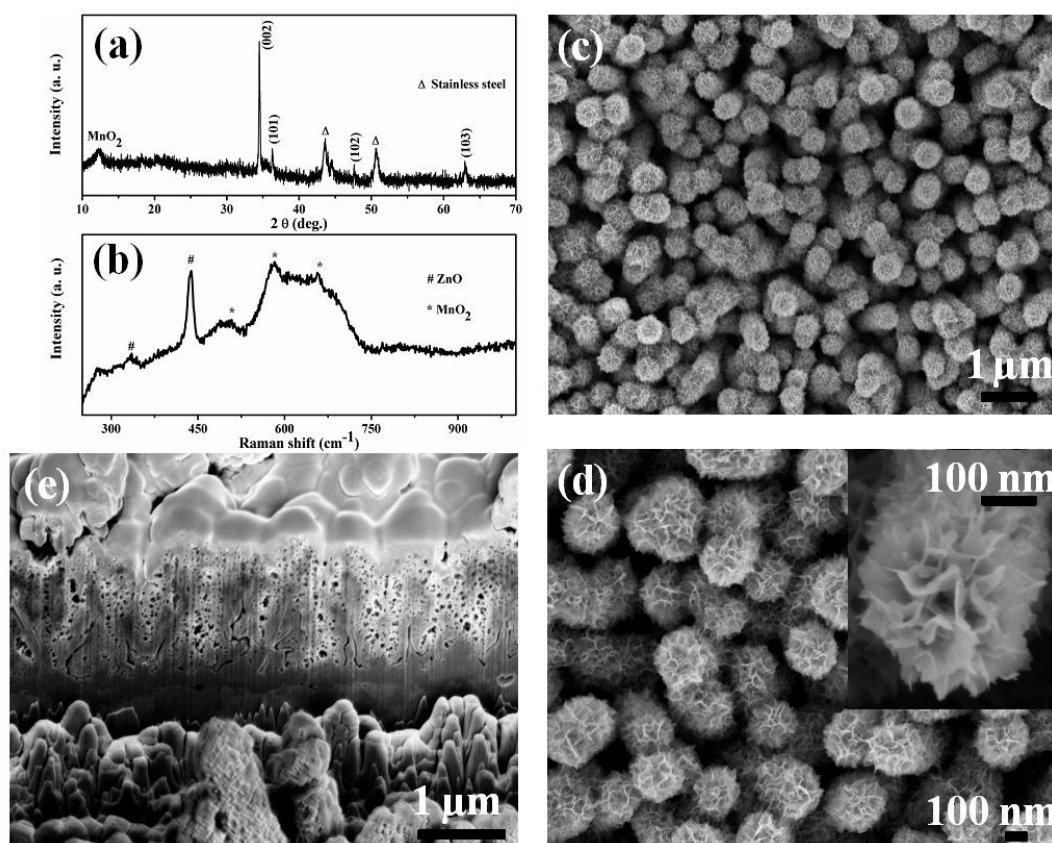


Figure 3. (a) XRD pattern and (b) Raman spectra of AZO@ MnO_2 hybrid core/shell arrays; (c, d) FESEM images of the AZO@ MnO_2 hybrid core/shell arrays with a high uniformity and regularity (Inset in Fig. 3(d) is an enlarged image of an individual nanostructure); and (e) cross-sectional image of the AZO@ MnO_2 hybrid structure.

Three characteristic peaks centered at 506, 565, and 648 cm^{-1} are detected for the birnessite-type MnO_2 . The Raman band at 648 cm^{-1} can be viewed as the symmetric stretching vibration (Mn-O) of the MnO_6 groups, and the band at 565 cm^{-1} is attributed to the (Mn-O) stretching vibration in the basal plane of MnO_6 sheets. Peaks centered around 332 and 437 cm^{-1} are two characteristic peaks in the vibrational spectrum of single-crystalline ZnO. No observable signals of carbon were found when the recording wavelength was extended up to 3000 cm^{-1} , indicating the complete consumption of carbon. Fig. 2(e) shows the Mn 2p XPS spectra of the AZO/ MnO_2 hybrid structure. Two peaks of Mn 2P_{3/2} and Mn 2P_{1/2} centered at 642.4 and 654.3 eV are observed, with a spin-energy separation of 11.9 eV. The binding energies are in good accordance with previous reports of Mn 2P_{3/2} and Mn 2P_{1/2} in MnO_2 [30], indicating the Mn ion in the product is present in the chemical state of Mn^{4+} .

Fig. 3(c) and (d) show the FESEM images of the AZO@ MnO_2 hybrid core/shell architecture on SS substrates. Highly branched and flaky MnO_2 nanosheets were coated uniformly on the AZO nanowire surfaces, forming a highly open and porous nanostructured surface morphology. This

morphology greatly increases the packing density and utilization of active materials and results in a high specific capacitance. Based upon the HR-FESEM observations, the thickness of nanosheet is estimated to be about 3-5 nm (see Supplementary Information), consistent with a previous report [23]. Cross-sectional image of AZO@MnO₂ obtained by the focused ion beam(FIB)-SEM technique is shown in Fig. 3(e), confirming porous structures not only on the top surface but also within the arrays. The open porous channels could increase the electrolyte-material contact and further facilitate the ionic diffusion through the electrode, both contributing to a higher specific capacitance and better high rate performances.

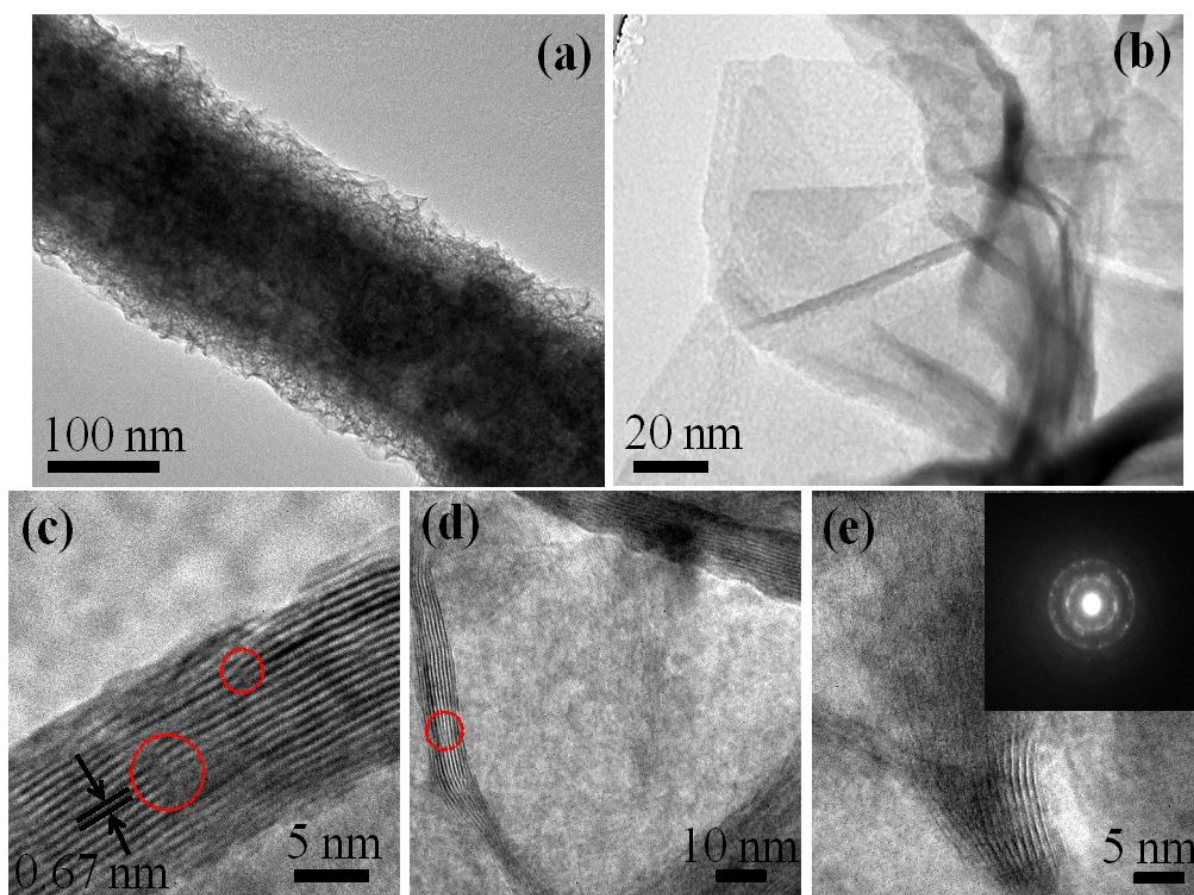


Figure 4. Microstructure characterization by TEM: (a) TEM image of an individual hybrid structure; (b) an enlarged image of several MnO₂ nanosheets from the hybrid structure; (c-e) HRTEM images of MnO₂ nanosheets. The red circled region in (c, d) indicates several dislocations.

Fig. 4 shows low-mag transmission electron microscopy (TEM) and high-resolution TEM (HRTEM) images of the AZO@MnO₂ nanowire arrays. High porous nanosheets uniformly cover the core AZO nanowire (Fig. 4(a) and (b)), in agreement with the SEM results. The HRTEM images in Fig. 4(c)-(e) show clear lattice fringes of polycrystalline structure with a spacing of ~ 0.67 nm corresponding to the (001) crystallographic planes of the birnessite-type MnO₂ [23]. The diffraction pattern shown in the inset of Fig. 4(e) also confirms a polycrystalline structure of the MnO₂

nanosheets. Dislocations are also noticed along the nanosheet direction (red circles in Fig. 4(c) and (d)), indicating the poor crystallinity of the MnO_2 nanosheets, which agrees well with the XRD results.

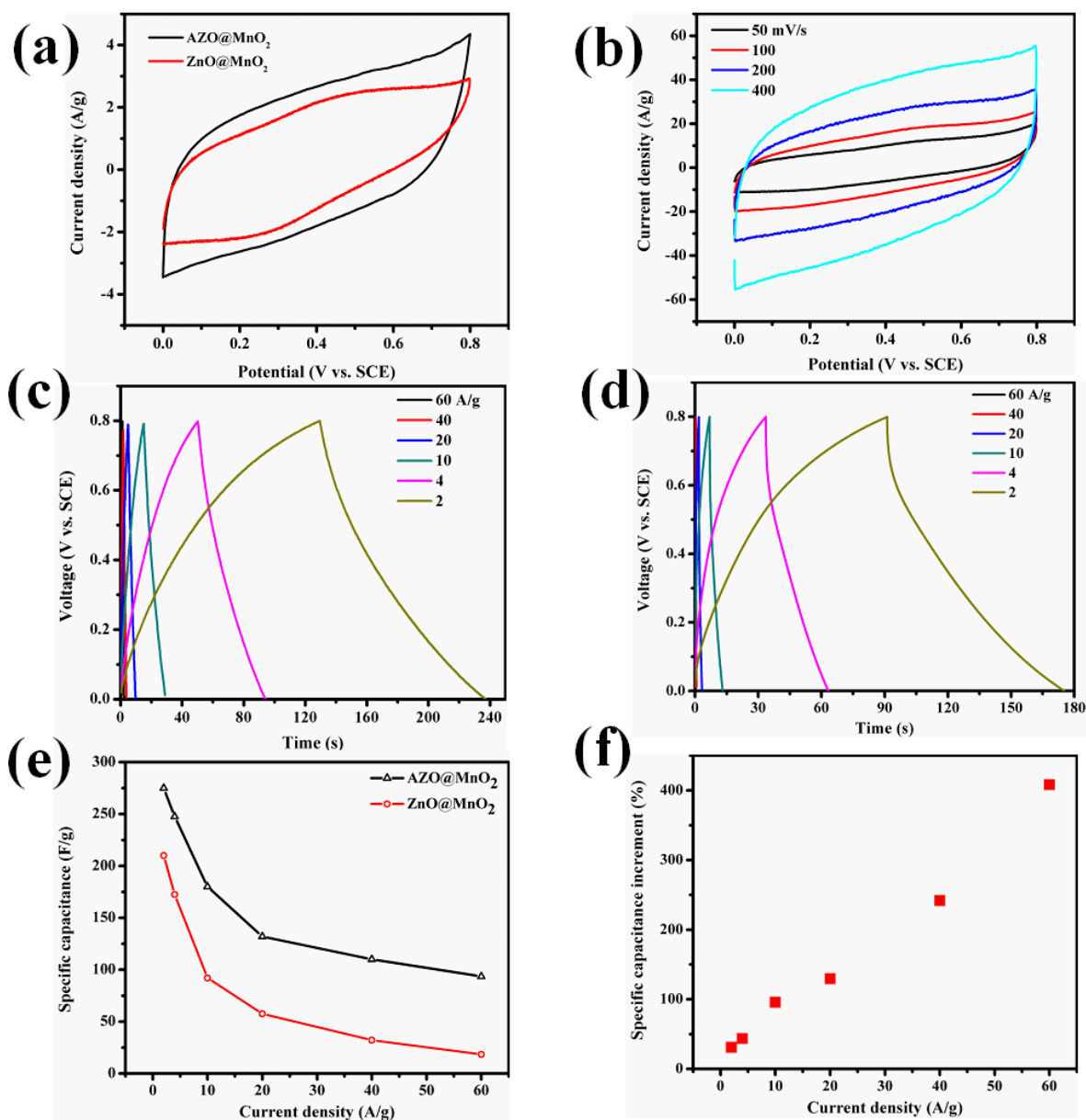


Figure 5. Electrochemical Performance of the AZO/ MnO_2 core shell electrodes: (a) CV curves at a scan rate of 10 mV/s; (b) CV curves at 50-400 mV/s for the AZO/ MnO_2 hybrid electrode; (c, d) Galvanostatic charge-discharge curves of the AZO/ MnO_2 and ZnO/ MnO_2 hybrid electrodes, respectively; (e) specific capacitances as a function of different current densities; and (f) specific capacitance increment as a function of different current densities.

The electrochemical capacitive performance of the AZO/ MnO_2 as well as the pure ZnO/ MnO_2 nanowire arrays were evaluated with the cyclic voltammogram (CV) and galvanostatic charge-discharge measurements. Fig. 5(a) shows the CV curves of the AZO/ MnO_2 and ZnO/ MnO_2

hierarchical hybrid arrays recorded in a 1 M Na₂SO₄ aqueous solution at a scan rate of 10 mV/s. The CV curve of AZO@MnO₂ is quasi-rectangular and symmetric in shape without obvious redox peaks, reflecting ideal pseudocapacitive behavior [48]. The pseudocapacitive electrochemical performance of the AZO@MnO₂ outperforms that of ZnO@MnO₂ as referred from a more ideal CV profile and larger CV integrated area. The specific capacitance (C_{sp}) of the electrode can be calculated from CV curves according to the following equation:

$$C_{sp} = \frac{Q}{\Delta V \cdot m} \quad (2)$$

where C (F/g) is the specific capacitance, m (g) is the mass of the total electrode materials (or mass of the active materials), Q (C) is the average charge during the charging and discharging process, and ΔV (V) is the potential window.

At a scan rate of 10 mV/s, a high specific capacitance of 213 F/g (based on total electrode mass, ~355 F/g based on MnO₂) was achieved from AZO@MnO₂; while the value is 151 F/g for ZnO@MnO₂ under the same conditions of measurement. To further investigate the electrochemical performances of AZO@MnO₂ and ZnO@MnO₂, higher rate capability experiments were carried out. Fig. 5(b) shows the cyclic voltammograms (CV) of AZO@MnO₂ measured at different sweep rates of 50, 100, 200 and 400 mV/s. The CV profiles retain a rectangular shape at all sweep rates without obvious redox peaks, indicating again the ideal pseudocapacitive nature as well as suitability for high rate operation of the AZO@MnO₂ hybrid electrode. At a high scan rate of 400 mV/s, the average specific capacitance was ~100 F/g, ~47% of that at 10 mV/s. This implies that even at higher scan rates, considerable active materials can still be electrochemically utilized. For comparison, the cyclic voltammograms of the ZnO@MnO₂ were measured at the same scan rates (see Supplementary Information). It is noted that the integrated area of the AZO@MnO₂ at the same scan rate is larger than that of ZnO@MnO₂, which suggests the AZO@MnO₂ has a higher specific capacitance as well as excellent rate capacitance properties.

Galvanostatic charge/discharge measurements were carried out on AZO@MnO₂ and ZnO@MnO₂ electrodes in the potential range of 0-0.8V at different current densities. The results were shown in Fig. 5(c) and (d), respectively. As can be seen from the constant current charge-discharge curves, the discharge time of AZO@MnO₂ electrode is substantially enhanced compared with ZnO@MnO₂ electrode and the charge/discharge curves for AZO@MnO₂ electrode show more symmetrical profiles than these of the ZnO@MnO₂ electrode, a result of the enhancement of the conductivity in the core supporting nanowires. The discharge specific capacitance can be calculated from the discharge curves by the following equation:

$$C_{sp} = \frac{I\Delta t}{m\Delta V} \quad (3)$$

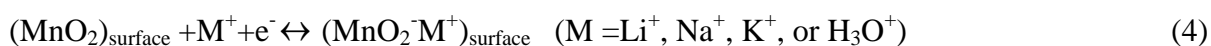
Where C_{sp} (F/g) is the specific capacitance, I is the discharging current, Δt is the discharging time, ΔV is the potential window, and m (g) is the mass of the total electrode materials (or mass of the active materials).

At a low current density of 2 A/g, the specific capacitances of AZO@MnO₂ and ZnO@MnO₂ are calculated to be about 275 (based on total electrode mass, ~458 F/g based on MnO₂) and 210 F/g, respectively. Fig. 5(e) shows the variation of the C_{sp} value as a function of current densities for the AZO@MnO₂ and ZnO@MnO₂ electrodes. It can be seen that the AZO@MnO₂ electrode not only delivers higher specific capacitances, but also maintain it at a high current density compared with the ZnO@MnO₂ electrode. As shown in Fig. 5(e), for AZO@MnO₂ hybrid electrode, a specific capacitance of 93.5 F/g (~35% retention) was retained as the rate changes from 2 to 60 A/g. While for ZnO@MnO₂ electrode, only 18.5 F/g (i.e., ~9% capacity retention) was achieved at a current density of 60 A/g. An over 400% specific capacitance increment was achieved at a high current density of 60 A/g (Fig. 5(f)), indicating a greatly improved rate performance for the Al-doping and hydrogenation of the ZnO as compared with pure ZnO nanowires.

AZO@MnO₂ electrode exhibited comparable or superior performance to other MnO₂-based composite materials such as Ag-loaded manganese oxide nanosheets (272 F/g at 10 mV/s) [49], MnO₂ nanoflower-CNTs composite arrays (199 F/g at a lower current density) [50], ultrafine MnO₂ nanowire network (279 F/g at 1A/g) [51], and graphene oxide-MnO₂ nanocomposites (111 F/g at 1A/g) [52]. Very recently, He *et al.* [30] reported the synthesis of electrodeposited ZnO nanorod/MnO₂ shell composites, which exhibited a specific capacitance as high as 405 F/g at a scan rate of 10 mV/s.

The performance of the hybrid AZO/MnO₂ is much higher than that of the pure manganese oxide nano-sheet electrodes (90 F/g at a scan rate of 10 mV/s) [49]. In the present work, since AZO@MnO₂ and ZnO@MnO₂ have almost the same surface morphologies, similar behavior in ion diffusion is expected. Therefore, the enhanced electrochemical performance could be caused by the improvement of conductivity in core-supporting nanowire material. The highly conductive AZO core functions as an optimized electron-conducting pathway, which could support fast electron transportation as required by high rate capability. By combining the characteristics of the two components, fast ion and electron transfers are accelerated in the unique AZO@MnO₂ hierarchical architecture.

In aqueous electrolytes, the charge storage mechanism of MnO₂ could be described by the following reaction:



It is reported that the charge storage is only involved the surface atoms of the MnO₂ crystallites or at a very thin layer [53]. AZO@MnO₂ exhibits a large specific surface area of electroactive MnO₂ material, in which numerous active sites are available for the adsorption of Na⁺ and possible intercalation/de-intercalation of Na⁺ [31]; hence a high specific capacitance could be expected. Therefore, highly porous and accessible ultrathin nanosheet shell structure can enhance the electrochemical utilization of active sites as well as enable fast and reversible faradic reactions by shortening the ion diffusion path. It is noteworthy that the overall capacitance of the electrode is

mainly contributed from active MnO₂ component. For one reason, ZnO has a small capacity [28,30]. For another, since ZnO were coated with porous MnO₂, electron transfer reaction (Faradaic reaction) mainly occurs at the surface of the electrode, and core material could rarely take part in the charge-storing process [26].

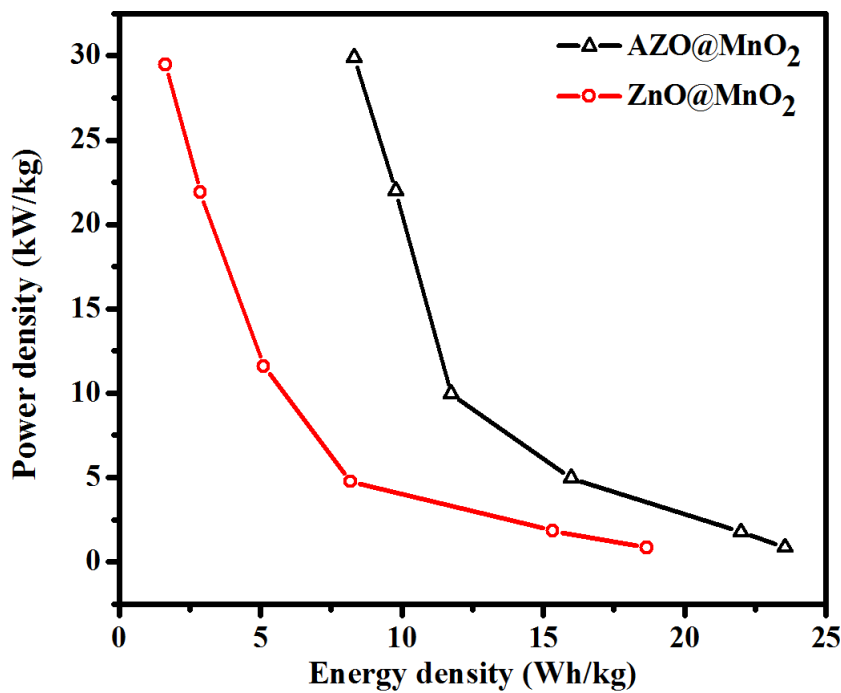


Figure 6. Ragone plot(power density vs. energy density) of the AZO@MnO₂ and ZnO@MnO₂ hybrid electrodes.

Fig. 6 shows the Ragone plot (power density vs energy density) of the AZO@MnO₂ and ZnO@MnO₂ electrodes. The power density and energy density are calculated from the following equations:

$$E = \frac{1}{2} C(\Delta V)^2 \tag{5}$$

$$P = \frac{E}{t}$$

Where E (Wh/kg). C (F/g), ΔV (V), t (s) and P (kW/kg) are the energy density, specific capacitance, potential window of discharge, discharge time and power density, respectively. The energy and power densities were calculated from charge-discharge curves at different current densities. The energy-power performance of the AZO@MnO₂ electrode is higher than that of the ZnO@MnO₂ because of a higher specific capacitance. For AZO@MnO₂, even at a high power density of ~30kW/kg, the energy density still reaches to be ~8.5 Wh/kg. At a lower power density of

~ 0.85 kW/kg, the energy density reaches as high as ~ 24 Wh/kg. While for pure ZnO@MnO₂, the power density can still reach ~ 30 kW/kg, but the energy density is as low as ~ 1.7 Wh/kg; at a lower power density of ~ 0.80 kW/kg, the energy density drops to ~ 18 Wh/kg. The AZO@MnO₂ hybrid electrode delivered a high energy density of 11.7 Wh/kg at a power density of ~ 12 Wh/kg, which is about 2.5 times larger than that of the pure ZnO@MnO₂. The comparison suggests that for AZO@MnO₂ electrode, higher energy densities could be attained while still maintaining the characteristic of high power density.

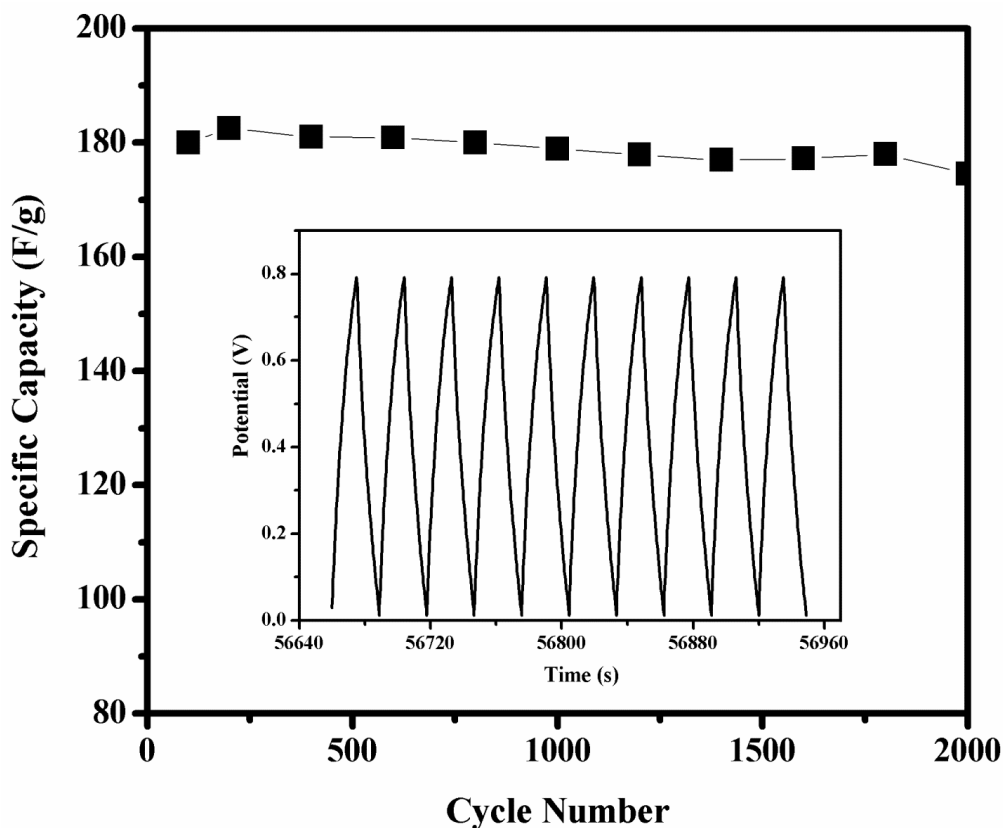


Figure 7. The specific capacitance as a function of cycle number at 10 A/g of the AZO@MnO₂ hybrid electrode. Inset shows the last 10 charge-discharge curve of the hybrid electrode.

To evaluate the durability of the AZO@MnO₂ hybrid electrode, cycling capability test was carried out at a high charge-discharge current density of 10 A/g using the constant current galvanostatic charge/discharge cycling technique in the potential window ranging from 0 to 0.8 V. Fig. 7 shows the specific capacitance retention of the AZO@MnO₂ hybrid electrode as a function of charge/discharge cycling numbers. The specific capacitance increases slightly at first and then decreases less than 3% in capacitance after 2000 charge-discharge cycles. The cycling stability of AZO@MnO₂ hybrid electrode is superior to pure MnO₂ and MnO₂-GO composites [51]. The last 10 cycles (inset in Fig. 7) exhibit highly symmetric charge/discharge characteristics, confirming the excellent long-term cyclability of the hybrid electrode. Excellent cycling stability was also

demonstrated on nickel hydroxidenitrate nanoflakes-coated ZnO nanowire arrays [28], proving the good durability and integrity of the hierarchical architecture.

4. CONCLUSIONS

In summary, Al-doped and hydrogenated ZnO nanowire arrays were used as supporting backbone infrastructures in fabricating AZO@MnO₂ hybrid core/shell electrode. The unique architecture of AZO@MnO₂ hybrid electrode offers high surface area, fast ion transportation, and good electronic conductivity, resulting in superior electrochemical performances (high specific capacitances, excellent rate capability and cycle stability). The hybrid AZO/MnO₂ core/shell electrode displays simultaneously-enhanced energy and power densities as compared with the pure ZnO/MnO₂ electrode. The extraordinary supercapacitor performance and the cost-effective and scalable synthesis approach suggest that AZO@MnO₂ hybrid electrode could be considered as promising electrode material for supercapacitor applications. Taking advantage of both highly electrochemical active MnO₂ nanosheets and highly conductive core nanowires as electron conducting pathways, the doping and hydrogenation approach reported here can be applied in the fabrication of other promising TO_x@MnO₂ (T = Ti, Sn, Fe, W, Cu, Ag, Ir, Ru, etc.) core/shell electrodes for further improvement of the electrical conductivity and capacitive performance for electrochemical energy storage applications.

ACKNOWLEDGEMENTS

This work was supported by a NSF career award under the Award number of DMR 1151028. The author Mingpeng Yu thanks for the financial support from China Scholarship Council (CSC File No. 2010646040).

References

1. R. Kötz and M. Carlen, *Electrochim. Acta* 45 (2000) 2483.
2. L. L. Zhang and X. S. Zhao, *Chem. Soc. Rev.* 38 (2009) 2520.
3. J. Biener, M. Stadermann, M. Suss, M. A. Worsley, M. M. Biener, K. A. Rose and T. F. Baumann, *Energy Environ. Sci.* 4 (2011) 656.
4. H. Wang, Q. Hao, X. Yang, L. Lu and X. Wang, *Electrochem. Commun.* 11 (2009) 1158.
5. L. Nyholm, G. Nyström, A. Mihranyan and M. Strømme, *Adv. Mater.* 23 (2011) 3751.
6. L. Cao, F. Xu, Y. Y. Liang and H. L. Li, *Adv. Mater.* 16 (2004) 1853.
7. C. C. Hu, K. H. Chang, M. C. Lin and Y. T. Wu, *Nano Lett.* 6 (2006) 2690.
8. X. H. Lu, D. Z. Zheng, T. Zhai, Z. Q. Liu, Y. Y. Huang, S. L. Xie and Y. X. Tong, *Energy Environ. Sci.* 4 (2011) 2915.
9. M. D. Stoller and R. S. Ruoff, *Energy Environ. Sci.* 3 (2010) 1294.
10. E. Kang, Y. S. Jung, A. S. Cavanagh, G. H. Kim, S. M. George, A. C. Dillon, J. K. Kim and J. Lee, *Adv. Funct. Mater.* 21 (2011) 2430.
11. G. Lota, K. Fic and E. Frackowiak, *Energy Environ. Sci.* 4 (2011) 1592.
12. Y. G. Guo, J. S. Hu and L. J. Wan, *Adv. Mater.* 20 (2008) 2878.
13. A. Manthiram, A. Vadivel Murugan, A. Sarkar and T. Muraliganth, *Energy Environ. Sci.* 1 (2008) 621.

14. G. Yu, L. Hu, N. Liu, H. Wang, M. Vosgueritchian, Y. Yang, Y. Cui and Z. Bao, *Nano Lett.* 11 (2011) 4438.
15. Z. S. Wu, W. C. Ren, D. W. Wang, F. Li, B. L. Liu and H. M. Cheng, *ACS Nano* 4 (2010) 5835.
16. L. Hu, M. Pasta, F. L. Mantia, L. Cui, S. Jeong, H. D. Deshazer, J. W. Choi, S. M. Han and Y. Cui, *Nano Lett.* 10 (2010) 708.
17. Y. Hou, Y. Cheng, T. Hobson and J. Liu, *Nano Lett.* 10 (2010) 2727.
18. A. E. Fischer, K. A. Pettigrew, D. R. Rolison, R. M. Stroud and J. W. Long, *Nano Lett.* 7 (2007) 281.
19. W. Chen, Z. Fan, L. Gu, X. Bao and C. Wang, *Chem. Commun.* 46 (2010) 3905.
20. L. Chen, L. J. Sun, F. Luan, Y. Liang, Y. Li and X. X. Liu, *J. Power Sources* 195 (2010) 3742.
21. R. Liu and S. B. Lee, *J. Am. Chem. Soc.* 130 (2008) 2942.
22. S. Hashmi and H. Updahyaya, *Ionics* 8 (2002) 272.
23. J. Liu, J. Jiang, C. Cheng, H. Li, J. Zhang, H. Gong and H. J. Fan, *Adv. Mater.* 23 (2011) 2076.
24. C. Guan, J. Liu, C. Cheng, H. Li, X. Li, W. Zhou, H. Zhang and H. J. Fan, *Energy Environ. Sci.* 4 (2011) 4496.
25. L. Bao, J. Zang and X. Li, *Nano Lett.* 11 (2011) 1215.
26. J. Yan, E. Khoo, A. Sumboja and P. S. Lee, *ACS Nano* 4 (2010) 4247.
27. J. S. Ye, H. F. Cui, X. Liu, T. M. Lim, W. D. Zhang and F. S. Sheu, *Small* 1 (2005) 560.
28. J. Liu, C. Cheng, W. Zhou, H. Li and H. J. Fan, *Chem. Commun.* 47 (2011) 3436.
29. G. R. Li, Z. L. Wang, F. L. Zheng, Y. N. Ou and Y. X. Tong, *J. Mater. Chem.* 21 (2011) 4217.
30. Y. B. He, G. R. Li, Z. L. Wang, C. Y. Su and Y. X. Tong, *Energy Environ. Sci.* 4 (2011) 1288.
31. H. Jiang, L. Yang, C. Li, C. Yan, P. S. Lee and J. Ma, *Energy Environ. Sci.* 4 (2011) 1813.
32. G. Zimmermann, M. Lange, B. Q. Cao, M. Lorenz and M. Grundmann, *Phys. Status Solidi - R* 4 (2010) 82.
33. Y. Natsume and H. Sakata, *Mater. Chem. Phys.* 78 (2003) 170.
34. M. Ohyama, H. Kozuka and T. Yoko, *J. Am. Ceram. Soc.* 81 (1998) 1622.
35. C. G. Van de Walle, *Phys. Rev. Lett.* 85 (2000) 1012.
36. C. H. Hsu and D. H. Chen, *Nanotechnology* 21 (2010) 285603.
37. B. L. Zhu, J. Wang, S. J. Zhu, J. Wu, R. Wu, D. W. Zeng and C. S. Xie, *Thin Solid Films* 519 (2011) 3809.
38. G. Wang, H. Wang, Y. Ling, Y. Tang, X. Yang, R. C. Fitzmorris, C. Wang, J. Z. Zhang and Y. Li, *Nano Lett.* 11 (2011) 3026.
39. H. S. Jang, S. O. Kang and Y. I. Kim, *Solid State Commun.* 140 (2006) 495.
40. Y. L. Wang, H. S. Kim, D. P. Norton, S. J. Pearton and F. Ren, *Electrochem. Solid-State Lett.* 11 (2008) H88.
41. X. H. Lu, G. M. Wang, T. Zhai, M. H. Yu, J. Y. Gan, Y. X. Tong and Y. Li, *Nano Lett.* 12 (2012) 1690.
42. C. Kilic and A. Zunger, *Appl. Phys. Lett.* 81 (2002) 73.
43. X. Jin, W. Zhou, S. Zhang and G. Z. Chen, *Small* 3 (2007) 1513.
44. B. H. Hong, Y. C. Jung, J. S. Rieh, S. W. Hwang, K. H. Cho, K. H. Yeo, S. D. Suk, Y. Y. Yeoh, M. Li, D. W. Kim, D. Park, K. S. Oh and W. S. Lee, *Ieee T. Nanotechnol.* 8 (2009) 713.
45. Y. Geng, L. Guo, S. S. Xu, Q. Q. Sun, S. J. Ding, H. L. Lu and D. W. Zhang, *J. Phys. Chem. C* 115 (2011) 12317.
46. E. De la Rosa, S. Sepulveda-Guzman, B. Reeja-Jayan, A. Torres, P. Salas, N. Elizondo and M. J. Yacaman, *J. Phys. Chem. C* 111 (2007) 8489.
47. J. P. Liu, J. Jiang, M. Bosman and H. J. Fan, *J. Mater. Chem.* 22 (2012) 2419.
48. P. Simon and Y. Gogotsi, *Nat. Mater.* 7 (2008) 845.
49. G. N. Zhang, L. Zheng, M. Zhang, S. H. Guo, Z. H. Liu, Z. P. Yang and Z. L. Wang, *Energy Fuels* 26 (2012) 618.
50. H. Zhang, G. Cao, Z. Wang, Y. Yang, Z. Shi and Z. Gu, *Nano Lett.* 8 (2008) 2664.

51. H. Jiang, T. Zhao, J. Ma, C. Yan and C. Li, *Chem. Commun.* 47 (2011) 1264.
52. S. Chen, J. Zhu, X. Wu, Q. Han and X. Wang, *ACS Nano* 4 (2010) 2822.
53. M. Toupin, T. Brousse and D. Bélanger, *Chem. Mater.* 16 (2004) 3184.

Support information:

The ZnO seed layers (about 20 nm in thickness) were coated on the stainless steel substrate by sputtering method. ZnO nanowire arrays were grown by immersing the seeded stainless steel substrate into in a precursor solution containing 25 mM zinc nitride and 25mM hexamethylenetetramine (HMTA) at 85 °C for 5 h in a 45 mL teflon-lined stainless steel autoclave (Parr, 4049). As the doping source, aluminum nitrate nonahydrate ($\text{Al}(\text{NO}_3)_3 \cdot 9\text{H}_2\text{O}$) was added in the precursor solution. Al doping concentration (the atom ratio of Al to Zn) was chosen to be 20 at.%.

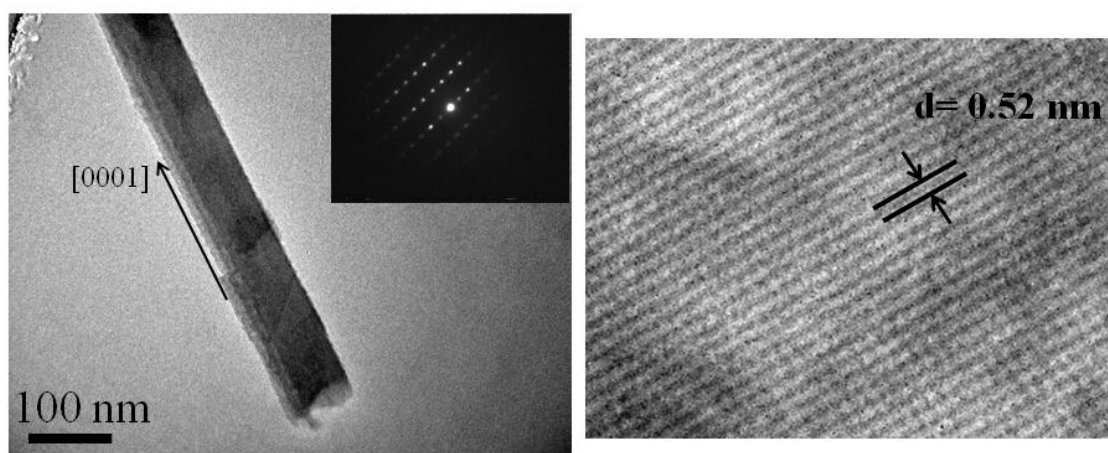


Figure S1. Typical TEM and HRTEM images as well as electron *diffraction pattern* of a single AZO nanowire. The HRTEM image confirms the single-crystal structure of the AZO nanowire and also demonstrates the lattice spacing of 0.52 nm in accordance with the *c* lattice constant of ZnO, indicating that the nanowire growth direction is along the *c* axis.

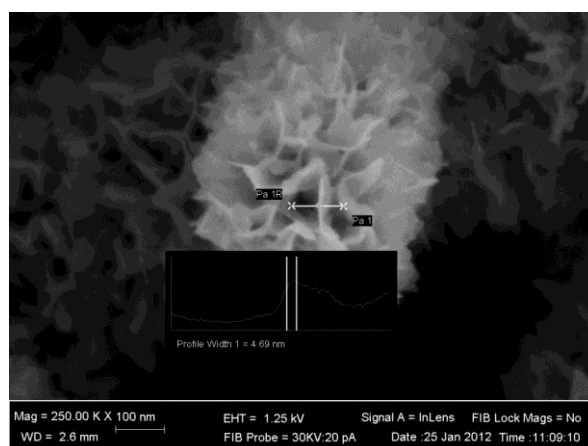


Figure S2. HR-FESEM observation of a single piece of MnO_2 nanosheet.

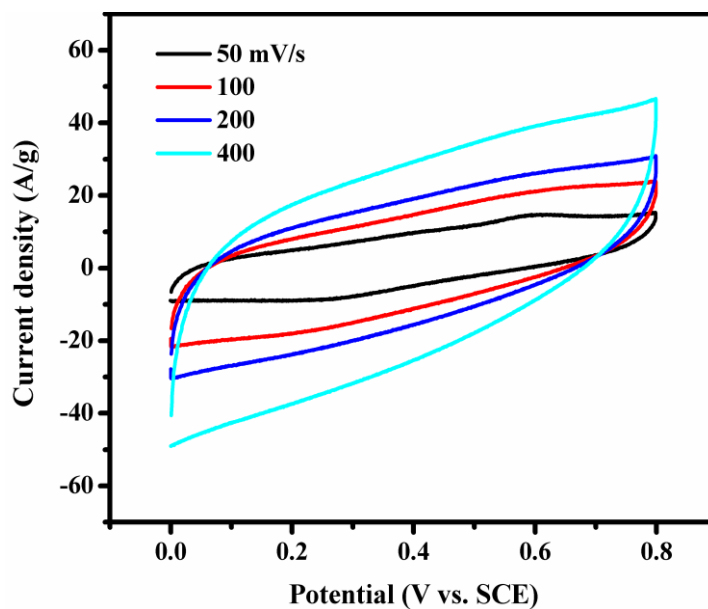


Figure S3. CV curves at 50-400 mV/s for ZnO@MnO₂ electrode.